

## Filaments of uniform quasi-geostrophic potential vorticity in pure strain

Jean N. Reinaud

To cite this article: Jean N. Reinaud (2023): Filaments of uniform quasi-geostrophic potential vorticity in pure strain, Geophysical & Astrophysical Fluid Dynamics, DOI: [10.1080/03091929.2023.2232939](https://doi.org/10.1080/03091929.2023.2232939)

To link to this article: <https://doi.org/10.1080/03091929.2023.2232939>



© 2023 The Author(s). Published by Informa UK Limited, trading as Taylor & Francis Group.



Published online: 16 Jul 2023.



Submit your article to this journal [↗](#)



View related articles [↗](#)



View Crossmark data [↗](#)

# Filaments of uniform quasi-geostrophic potential vorticity in pure strain

Jean N. Reinaud 

Mathematical Institute, University of Saint Andrews, St Andrews, UK

## ABSTRACT

Three-dimensional filaments of quasi-geostrophic potential vorticity are generic features of atmospheric and oceanic flows. They are often generated during the strong interactions between three-dimensional quasi-geostrophic vortices. They contribute to a direct cascade of enstrophy in spectral space. These filaments correspond to shear zones. Therefore they may be sensitive to shear instabilities akin to the Kelvin–Helmholtz instability of the classical two-dimensional vorticity strip. They are, however, often subjected to a straining flow induced by the surrounding vortices. This straining flow affects their robustness. This paper focuses on a simplified model of this situation. We consider the effect of a pure strain on a three-dimensional filament of uniform quasi-geostrophic potential vorticity. We first consider a quasi-static situation where the strain, assumed small, only affects the cross-sectional shape of the filament, but not the velocity field. We address the linear stability of the filament in that context and also show examples of the filament's nonlinear evolution. We then consider the linearised dynamics of the filament in pure strain. In particular we focus on the maximum perturbation amplification observed in the filament. We conclude that small to moderate strain rates are efficient at preventing a large perturbation growth. Nonlinear effects can nevertheless lead to the roll-up of weakly strained filaments.

## ARTICLE HISTORY


Received 8 April 2023  
Accepted 30 June 2023

## KEYWORDS

Vortex dynamics;  
quasi-geostrophy

## 1. Introduction

Three-dimensional filaments abound in eddy-driven atmospheric and oceanic flows. They often are the results of strong interactions between coherent masses of potential vorticity. For example, in geostrophic turbulence, the energy predominantly cascades towards large scales via the formation of large vortices by merger. These mergers generate a plethora of small-scale debris and filaments (Reinaud *et al.* 2003). These small-scale structures feed a direct cascade of enstrophy. In general, any strong vortex interaction is accompanied by the formation of filaments, see, e.g. Bambrey *et al.* (2007) and Reinaud and Dritschel (2009). These filaments are shear zone, hence are sensitive to shear instabilities akin to the Kelvin–Helmholtz instability. Yet, filaments are typically relatively long lived. Their longevity has been linked to the fact they are subjected to a straining flow induced by the surrounding vortices (Dritschel *et al.* 1991, Kevlahan and Farge 1997).

**CONTACT** Jean N. Reinaud  jean.reinaud@st-andrews.ac.uk, jnr1@st-andrews.ac.uk

© 2023 The Author(s). Published by Informa UK Limited, trading as Taylor & Francis Group.

This is an Open Access article distributed under the terms of the Creative Commons Attribution License (<http://creativecommons.org/licenses/by/4.0/>), which permits unrestricted use, distribution, and reproduction in any medium, provided the original work is properly cited. The terms on which this article has been published allow the posting of the Accepted Manuscript in a repository by the author(s) or with their consent.

The stability of a two-dimensional vorticity filament in an incompressible straining flow was investigated by Dritschel *et al.* (1991). The authors concluded that a pure strain has a stabilising effect of the filament. The stabilising mechanism is twofold. On the one hand, the strain increases the longitudinal perturbation wavelength as the filament is stretched and the growth rate of instabilities goes to zero as the perturbation wavelength goes to infinity. On the other hand, the longitudinal stretching of the filament is associated with a decrease in the spanwise direction of the amplitude of the perturbation, from incompressibility. A similar study was conducted by Harvey and Ambaum (2010) for a filament of potential temperature anomaly in a surface quasi-geostrophic model. Here the situation is different as the decrease of the width of the filament of potential temperature increases the shear inside the filament. This, in turn, increases the growth rate of the instability. The authors conclude that overall the strain has a destabilising effect.

In this paper, we consider three-dimensional filaments of uniform quasi-geostrophic potential vorticity in pure strain. This paper is organised as follows. The quasi-geostrophic model is presented in section 2. We first address the linear stability of the filament in section 3 in a quasi-static strain. Examples of the nonlinear evolution of the filament are also provided. We then consider the linearised dynamics of the filament in pure strain in section 4. We find that the strain eventually tends to stabilise the filament. Irreversible nonlinear effects can nonetheless lead to the rollup of the filament if the strain is weak. Finally conclusions are given in section 5. An appendix contains further information on the numerical convergence of the linear stability analysis.

## 2. Quasi-geostrophic model

The quasi-geostrophic (QG) model is the simplest dynamical model which captures the leading order features of rapidly-rotating, stably-stratified flows. In the form used in this study, it stems from a first-order Rossby number expansion of the three-dimensional Euler's equations in a rotating reference frame, for a stratified fluid under the Boussinesq approximation. The Rossby number is  $Ro = U/(fL)$ , where  $U$  is a typical horizontal velocity scale,  $f$  is the Coriolis frequency and  $L$  is a typical horizontal length scale. Specifically, the QG model is valid when  $Fr^2 \ll Ro \ll 1$ , where  $Fr = U/(NH)$  is the Froude number,  $N$  is the buoyancy (or Brunt-Väisälä) frequency and  $H$  is a typical vertical length scale. A detailed derivation of the model may be found in chapter 5, section 5.5 of Vallis (2006). The flow fields can be recovered from a single scalar field,  $q$ , the QG potential vorticity anomaly (PV), together with the possible addition of a potential flow. The PV,  $q$ , may be defined from a scalar stream function  $\varphi$  as

$$q = \frac{\partial^2 \varphi}{\partial x^2} + \frac{\partial^2 \varphi}{\partial y^2} + \frac{\partial^2 \varphi}{\partial z^2}, \quad (1)$$

where  $x$  and  $y$  are the horizontal coordinates and  $z = z_p N/f$  is a stretched vertical coordinate. Here  $z_p$  is the physical vertical coordinate and both  $N$  and  $f$  are assumed constant.

In the absence of adiabatic or dissipative effects,  $q$  is materially conserved,

$$\frac{\partial q}{\partial t} + \mathbf{u} \cdot \nabla q = 0. \quad (2)$$

$\mathbf{u}$  is the advecting velocity field

$$\mathbf{u} = (u, v, 0) = (u_g, v_g, 0) + (u_p, v_p, 0), \quad (3)$$

where

$$(u_g, v_g, 0) = \left( -\frac{\partial \varphi}{\partial y}, \frac{\partial \varphi}{\partial x}, 0 \right) \quad (4)$$

is the horizontal, non-divergent, advective geostrophic velocity, and  $\mathbf{u}_p = \nabla \Phi_p = (u_p, v_p, 0)$  is an additional potential flow. In the QG model, the vertical velocity is not, strictly speaking, zero, but is too small in the Rossby number expansion to contribute to the advection of PV. Equation (1) can be formally inverted using the appropriate Green's function, which in an unbounded domain (and without taking the potential part into account)

$$\varphi(\mathbf{x}) = -\frac{1}{4\pi} \iiint \frac{q(\mathbf{x}')}{|\mathbf{x} - \mathbf{x}'|} d^3 \mathbf{x}'. \quad (5)$$

In this paper, we consider filaments of PV subject to a horizontal potential strain,

$$\Phi_p = \frac{\gamma}{2}(x^2 - y^2), \quad (u_p, v_p, 0) = \gamma(x, -y, 0), \quad (6)$$

where  $\gamma$  is the constant strain rate.

### 3. Filament in strain: the quasi-static approach

We first analyse the linear stability of a PV filament quasi-statically deformed by the strain. In this context, we will refer to a quasi-static filament for simplicity. This is an extension of the work by Reinaud (2020) where the linear stability of a cylindrical filament of PV, with a circular cross-section, in the absence of strain ( $\gamma = 0$ ) is addressed. Here, the basic state consists of a cylindrical filament of uniform potential vorticity  $q$ . The axis of the filament is the  $x$ -axis, and the vertical cross-section of the filament is an ellipse of semi-axis length  $a$  in the  $y$ -direction and  $b$  in the  $z$ -direction as shown in figure 1. The filament is infinite in the  $x$ -direction. For the unperturbed basic state the PV is independent of  $x$  and therefore the filament does not induce a transversal velocity  $\bar{v}_g$  on itself. As the filament is placed in the pure strain, the elliptical cross-section of the filament deforms such that

$$a(t) = a_0 \exp(-\gamma t), \quad (7)$$

where  $a_0 = a(t = 0)$  and while  $b$  remains constant due to the lack of vertical advection.

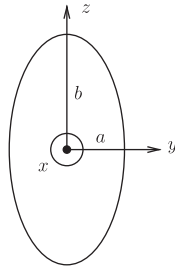


**Figure 1.** General geometry of the elliptical filament cross-section.

We first consider the quasi-static situation where  $\gamma \ll q$ . In this case, the potential velocities  $u_p$  and  $v_p$  are kinematically negligible. We investigate the stability of the filament for  $b$  fixed and various values of  $a$ , neglecting the time-dependence of  $a$  during the analysis. This allows to take into account the slow deformation of the filament, while neglecting the kinematic effects of  $u_p$  on its stability. This means taking  $\mathbf{u}_p = \mathbf{0}$  during the analysis.

The inner stream function for the elliptical filament can readily be adapted from the classical two-dimensional Kirchhoff vortex (Kirchhoff 1876, Lamb 1916):<sup>1</sup>

$$\bar{\varphi}(\mathbf{x}) = \frac{q}{2(a+b)} (by^2 + az^2) \quad (8)$$

$$\bar{u}_g(\mathbf{x}) = -\frac{qb}{(a+b)}y \quad (9)$$

It should be noted that the magnitude of shear rate inside the filament  $s = |q|b/(a+b) = |q|/(1+\lambda)$  depends on the aspect ratio  $\lambda = a/b$  of the filament's elliptical vertical cross-section. It increases as  $\lambda$  decreases, yet remains bounded,  $0 < s < |q|$ .

### 3.1. Linear stability

The linear stability analysis relies on the analysis of normal modes of deformation of the surface bounding the filament. Recall that we use  $\mathbf{u}_p = \mathbf{0}$  in the analysis in the quasi-static approach. The procedure is detailed in Reinaud (2020). The boundary of the unperturbed filament is first parametrised

$$\bar{y} = a \cos(\theta), \quad \bar{z} = b \sin(\theta) \quad (10)$$

where  $-\pi/2 \leq \theta < 3\pi/2$ . Then the contours are perturbed in the  $y$ -direction by a monochromatic wave

$$y = \bar{y} + \epsilon \eta(x, \theta, t) = \bar{y} + \epsilon \operatorname{Re} \left\{ \hat{\eta}(\theta) \exp(i(kx - \sigma t)) \right\} \quad (11)$$

where  $k \in \mathbb{R}$  is the perturbation wavenumber,  $\hat{\eta} \in \mathbb{C}$  is the complex amplitude of the perturbation and  $\sigma = \sigma_r + i\sigma_i \in \mathbb{C}$  is the complex frequency. The imaginary part  $\sigma_i$  of the complex frequency is consequently the mode's growth rate.

The linearised kinematic boundary condition, at order  $\epsilon$ , is

$$\frac{\partial \eta(\theta)}{\partial t} + \bar{u}_g \frac{\partial \eta(\theta)}{\partial x} = v_g(x, \bar{y}(\theta), \bar{z}(\theta), t) \quad (12)$$

where the transversal velocity perturbation is obtained by contour integration

$$v_g(x, \bar{y}(\theta), \bar{z}(\theta), t) = -\frac{qik}{4\pi} \int_{-\pi/2}^{3\pi/2} 2\eta(\theta') K_0(k\rho) b \cos(\theta') d\theta' \quad (13)$$

and  $\rho = \sqrt{(\bar{y}(\theta) - \bar{y}(\theta'))^2 + (\bar{z}(\theta) - \bar{z}(\theta'))^2}$ , and  $K_0$  is the modified Bessel function of the second kind and zeroth order. The full derivation of equation (13) is given in Reinaud (2020) for  $a = b = 1$ . The surface of the filament is then discretised by  $n$  points

$$\bar{y}_i = a \cos \theta_i, \quad \bar{z}_i = b \sin \theta_i \quad (14)$$

<sup>1</sup> Chap. XX, section 4, p.261 of Kirchhoff (1876), section 159, p.226 of Lamb (1916)

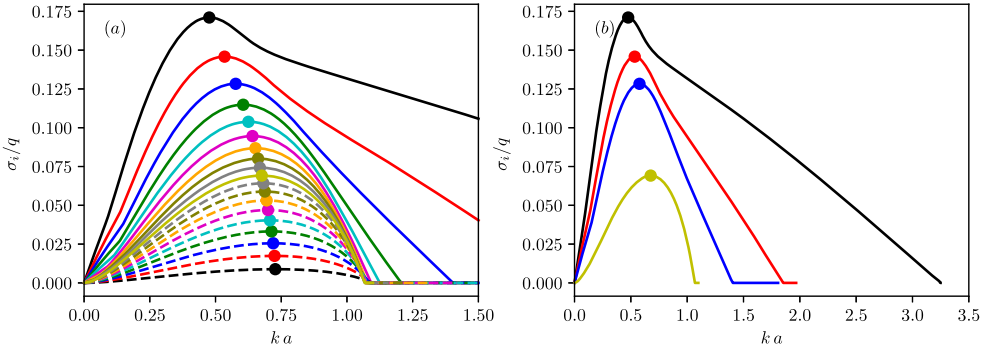


**Figure 2.** (a) Largest normalised growth rate  $\sigma_i/q$  versus the non-dimensional wavenumber  $ka$ , for  $\lambda = 0.1$  (solid black),  $0.2$  (solid red),  $0.3$  (solid blue),  $0.4$  (solid green),  $0.5$  (solid cyan),  $0.6$  (solid magenta),  $0.7$  (solid orange),  $0.8$  (solid olive),  $0.9$  (solid grey),  $1$  (solid yellow),  $0.9^{-1}$  (dashed grey),  $0.8^{-1}$  (dashed olive),  $0.7^{-1}$  (dashed orange),  $0.6^{-1}$  (dashed magenta),  $0.5^{-1}$  (dashed cyan),  $0.4^{-1}$  (dashed green),  $0.3^{-1}$  (dashed blue),  $0.2^{-1}$  (dashed red),  $0.1^{-1}$  (dashed black). The circle indicates the location of the maximum growth rate. (b): same but showing an extended range of  $ka$  for  $\lambda = 0.1, 0.2, 0.3$  and  $1$ . (Colour online.)

**Table 1.** Values of  $k_m a$ ,  $k_c a$ ,  $\sigma_{i,\max}/q$  for all  $\lambda$  considered.

$\lambda$	$k_c a$	$k_m a$	$\sigma_{i,\max}/q$	$\lambda$	$k_c a$	$k_m a$	$\sigma_{i,\max}/q$
0.1	3.244	0.476	0.171	$0.9^{-1}$	1.068	0.682	0.0642
0.2	1.850	0.534	0.146	$0.8^{-1}$	1.069	0.688	0.0589
0.3	1.403	0.577	0.128	$0.7^{-1}$	1.071	0.694	0.0531
0.4	1.207	0.605	0.115	$0.6^{-1}$	1.074	0.700	0.0470
0.5	1.125	0.625	0.104	$0.5^{-1}$	1.078	0.707	0.0403
0.6	1.091	0.641	0.0946	$0.4^{-1}$	1.081	0.713	0.0332
0.7	1.077	0.652	0.0868	$0.3^{-1}$	1.086	0.719	0.0255
0.8	1.071	0.662	0.0801	$0.2^{-1}$	1.091	0.724	0.0174
0.9	1.068	0.669	0.0742	$0.1^{-1}$	1.094	0.727	0.00883
1.0	1.067	0.676	0.0692				

where  $\theta_i = -\pi/2 + (i - 0.5)\Delta\theta$ , with  $\Delta\theta = 2\pi/n$  and  $1 \leq i \leq n$ . The integration in (13) between the nodes  $\theta'_i$  and  $\theta'_{i+1}$  is done by two-point Gaussian quadrature. The discretised version of equation (12) leads to a  $n$ -dimensional eigenvalue problem where  $\sigma$  is the complex eigenvalue and  $\hat{\boldsymbol{\eta}} = (\hat{\eta}_i)_{1 \leq i \leq n}$  is the complex eigenvector. In practice, we set  $ab = 1$  without loss of generality and vary  $\lambda = a/b$ . In practice, we use  $n = 2000$ . A note on accuracy is presented in appendix.

We investigate 19 values for  $\lambda$ , first  $\lambda = 0.1i$ ,  $1 \leq i \leq 10$ , then  $\lambda = (0.1i)^{-1}$ ,  $1 \leq i \leq 9$ . Figure 2 shows the largest normalised growth rate  $\sigma_i/q$  versus the normalised wavenumber  $ka$ . For all  $\lambda$  there is a range  $ka \in (0, k_c a)$  where  $\sigma_i > 0$  hence where the filament is unstable. The normalised cutoff wavenumber  $k_c a$  depends on  $\lambda$ . The filament is marginally stable ( $\sigma_i = 0$ ) outside this range. The values of  $k_c a$  are reported in table 1 for clarity. For  $\lambda > 0.5$ ,  $1.067 \leq k_c a \leq 1.094$  varies little (i.e. a variation of about 2.5%). It, however, increases significantly as  $\lambda \leq 0.5$  decreases. A further calculation shows that  $k_c a = 6.071$  for  $\lambda = 0.05$  (result not reported in table 1 nor in figure 2).

The normalised wavenumber of the most amplified mode  $k_m a$  slightly increases with  $\lambda$ . The growth rates and in particular the growth rate,  $\sigma_{i,\max} = \sigma_i(k_m)$  of the most amplified mode increases as  $\lambda$  decreases. Recall the intensity of the shear inside the filament increases

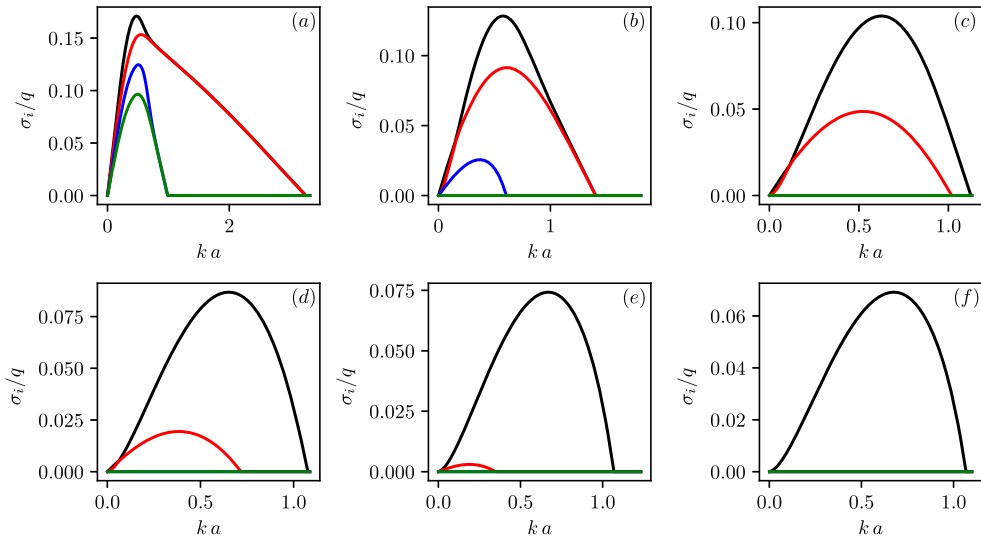


**Figure 3.** Normalised growth rates  $\sigma/q$  versus the non-dimensional wavenumber  $ka$ , for (a)  $\lambda = 0.1$ , (b)  $0.2$ , (c)  $0.3$ , (d)  $0.4$ , (e)  $0.5$ , (f)  $0.7$ , (g)  $0.9$ , (h)  $1.0$ . (a) 7 largest growth rates shown. (b)–(h) 4 largest growth rates shown. (Colour online.)

as  $\lambda$  decreases. It should be noted that  $\sigma_{i,\max}$  does not exactly scale as the inner shear rate  $s = q_0/(1 + \lambda)$ , since  $k_m$  also depends on  $\lambda$ .

For  $\lambda < 1$ , there is typically more than one unstable mode. Figure 3 shows the largest growth rates versus  $ka$ . For  $\lambda = 0.1$ , there are in fact up to seven unstable modes, shown in panel (a) of figure 3. As  $\lambda$  increases the maximum number of unstable modes decreases. There are only up to four unstable modes for  $\lambda = 0.2$  and three for  $\lambda = 0.3$ . The third unstable mode for  $\lambda = 0.4$  has a maximum growth rate of only  $\sigma_i/q = 1.05 \times 10^{-3}$  for  $ka = 0.13$ . Then there are up to two unstable for  $0.5 \leq \lambda \leq 0.9$ , and only one for  $\lambda \geq 1$ .

Figure 4 shows the shape of the perturbation eigenmodes on a vertical cross-section of the filament for  $kx = 2m\pi$ ,  $m \in \mathbb{Z}$  for  $ka = 0.6$  and  $\lambda = 0.1$ . Recall that the wave is perpendicular to  $(y, z)$ -plane shown in the figure. The most amplified unstable mode, corresponding to the largest growth rate mostly corresponds to a transversal displacement of the cross-section, hence indicative of a simple sinusoidal wave in the  $x$ -direction. Interestingly, the second most amplified mode corresponds to the tilting of the filament. This is connected to the tall column instability discovered by Dritschel (1996) and the tilt instability also observed in the interaction of prolate vortices by Reinaud and Dritschel (2005). The third and fourth most amplified modes are primarily associated with the deformation of the top and bottom tips of the filament. The fifth and sixth most amplified modes affect an even narrower region near the top and bottom tips of the filament. This shows the sensitivity of the filament tips to vertical shear as  $\lambda \rightarrow 0$ . For such a small  $\lambda$ , the curve of the largest instability growth rates has a long tail, with two modes having almost the same growth rate. This tail is absent for larger values of  $\lambda$ . An example of the perturbation eigenmodes is shown in figure 5 for the same value of  $\lambda = 0.1$  but  $ka = 2.23$ . The modes mostly, if not exclusively, affect the top tip or the bottom tip of the filament. This is confirmed in section 3.2 by a fully nonlinear simulation. For  $\lambda = 0.5$ , the largest instability

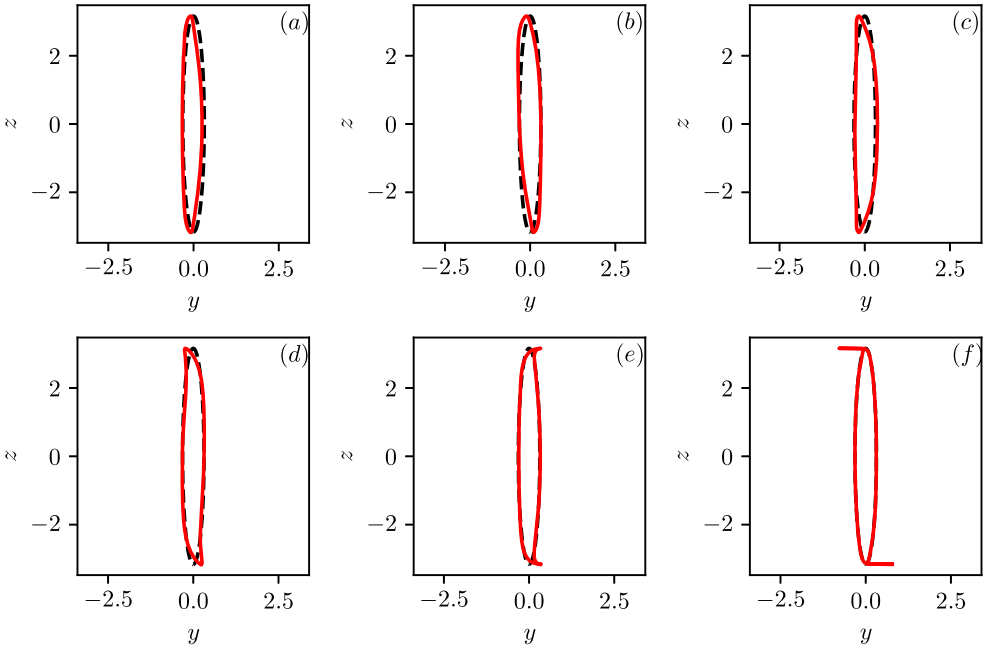


**Figure 4.** Normal mode perturbation  $\text{Re}\{\eta\}$  superimposed on the vertical cross-section of the filament's boundary (red contour) at  $kx = 2m\pi, m \in \mathbb{Z}$  for  $ka = 0.6$ , and undisturbed boundary (dashed black) for  $\lambda = 0.1$  and (a) largest growth rate, (b) second largest growth rate, (c) third largest growth rate, (d) fourth largest growth rate, (e) fifth largest growth rate, (f) sixth largest growth rate. (Colour online.)

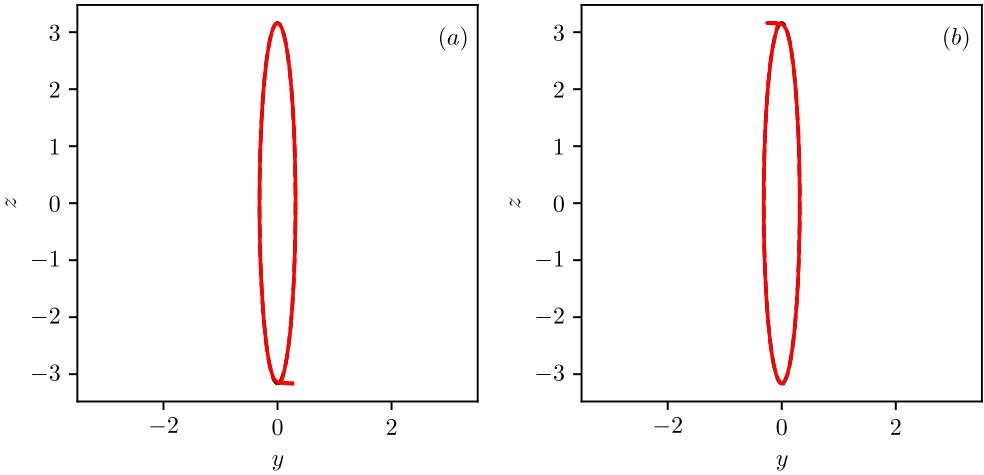


**Figure 5.** Normal mode perturbation  $\text{Re}\{\eta\}$  superimposed on the vertical cross-section of the filament's boundary (red contour) at  $kx = 2m\pi, m \in \mathbb{Z}$  for  $ka = 2.23$ , and undisturbed boundary (dashed black) for  $\lambda = 0.1$  and (a) largest growth rate, (b) second largest growth rate. (Colour online.)

growth rate corresponds again to a transversal displacement of the vertical cross-section of filament, as shown in figure 6(a) for  $ka = 0.6$ , corresponding to a simple wave in the  $x$ -direction. The second largest instability growth rate corresponds to an instability affecting preferentially the top and bottom tips of the vortex, with a small tilting of the filament, as shown in figure 6(b). For the unique unstable mode for  $\lambda = 1$ , the perturbation eigenmode



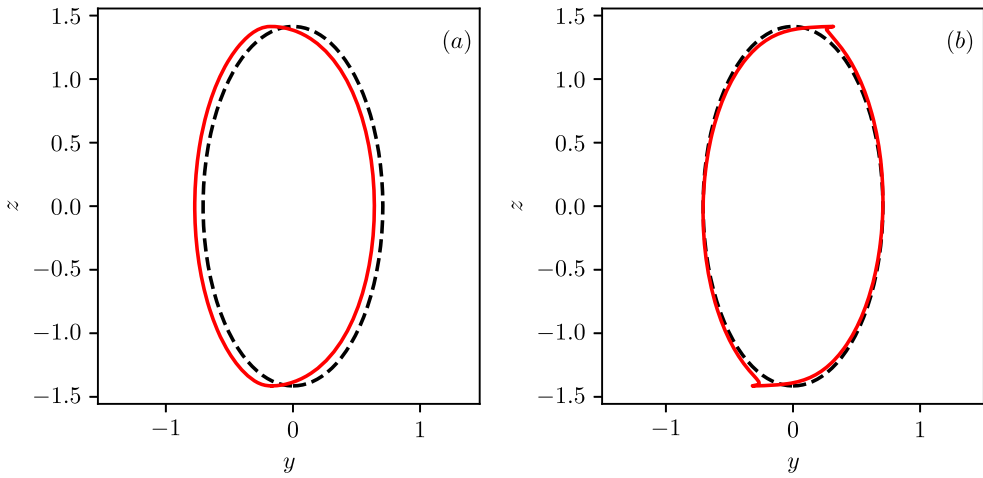


**Figure 6.** Normal mode perturbation  $\text{Re}\{\eta\}$  superimposed on the vertical cross-section of the filament's boundary (red contour) at  $kx = 2m\pi$ ,  $m \in \mathbb{Z}$  for  $ka = 0.6$ , and undisturbed boundary (dashed black) for  $\lambda = 0.5$ : (a) largest growth rate and (b) second largest growth rate. (Colour online.)

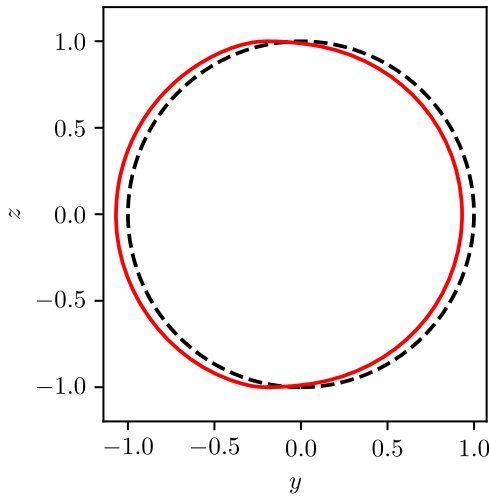


**Figure 7.** Normal mode perturbation  $\text{Re}\{\eta\}$  superimposed on the vertical cross-section of the filament's boundary (red contour) at  $kx = 2m\pi$ ,  $m \in \mathbb{Z}$  for  $ka = 0.6$ , and undisturbed boundary (dashed black) for  $\lambda = 1$ . (Colour online.)

corresponds to a lateral displacement of the vertical cross-section of filament, as shown in figure 7 for  $ka = 0.6$ .

### 3.2. Nonlinear evolution

We next consider the nonlinear evolution of an elliptical filament of vorticity. Again, no external strain is applied to the filament,  $\mathbf{u}_p = \mathbf{0}$ . The numerical simulations are performed using the Contour Advective Semi-Lagrangian algorithm (CASL) developed by Dritschel

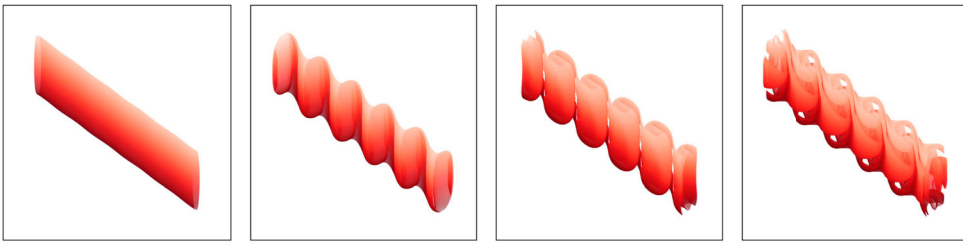


**Figure 8.** Filament's bounding contours from  $\lambda = 0.1$ , perturbed by a monochromatic wave  $k = 5$  ( $ka = 0.553$ ), at  $t = 0, 4, 6$  and  $8$ , viewed orthographically at an angle of  $45^\circ$  from the  $x$ -axis and the  $z$ -axis. Colour shading indicates depth (dark contours near the bottom of the filament and light contours). (Colour online.)

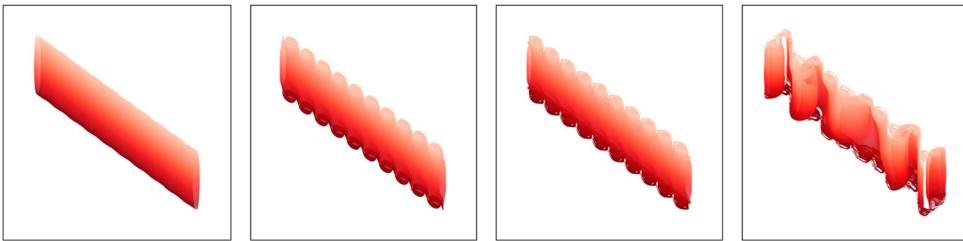


**Figure 9.** Filament's bounding contours from  $\lambda = 0.1$ , perturbed by a monochromatic wave  $k = 10$  ( $ka = 1.106$ ), at  $t = 0, 4, 6$  and  $14.5$ , viewed orthographically at an angle of  $45^\circ$  from the  $x$ -axis and  $z$ -axis. Colour shading indicates depth (dark contours near the bottom of the filament and light contours). (Colour online.)

and Ambaum (1997) and using the standard setup of the method. The domain is triply-periodic with dimensions  $[0, 2\pi]^3$ . The PV of the filament is set to  $q = 2\pi$ , implicitly defining a time scale for the flow. For comparison, a sphere of uniform PV as a turn over period of  $T = 6\pi/q$ . The axis of the filament is the  $y$ -axis in the simulations. We first consider a filament with  $a = 0.11$  and  $b = 1.1$  corresponding to  $\lambda = 0.1$ . Since there are multiple competing unstable modes for small  $ka$ , the contours bounding the filament are perturbed by a simple monochromatic sine wave of uniform amplitude rather than a specific eigenmode. The amplitude of the perturbation is  $\epsilon = 0.01$ . We first consider a perturbation with a normalised wavenumber  $ka = 0.332$ , corresponding to  $k = 3$  in the computational box. Results are presented in figure 12. As expected, the unstable filament rolls up to form Kelvin–Helmholtz-like three-dimensional billows. For  $ka = 0.553$ , corresponding to  $k = 5$  in the periodic computational box. This wave number is closer to the most amplified wavenumber ( $k_m a = 0.476$ ), compared to the previous case with  $ka = 0.332$ . Thus the roll-up occurs faster, as expected (figure 8).

For  $ka = 1.106$ , shown in figure 9, corresponding to  $k = 10$  in the computational box, the filament first developed 10 billows. However, modes with lower wavenumbers are more unstable than the perturbation introduced. The nonlinear evolution of the filament is enough to allow these modes to grow. In the late nonlinear evolution, these modes dominate the flow evolution. Some billows merge to form larger structures. This situation is more pronounced when initially forcing the filament with a perturbation with an even

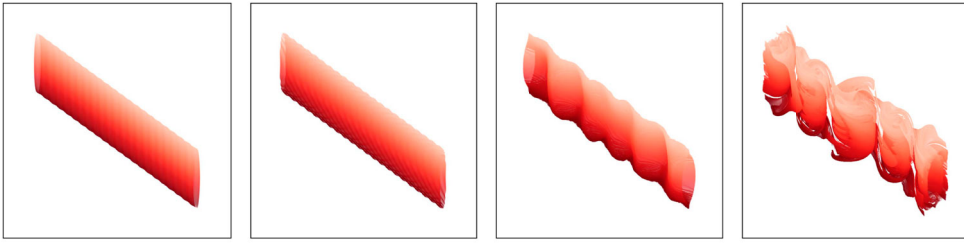


**Figure 10.** Filament's bounding contours from  $\lambda = 0.1$ , perturbed by a monochromatic wave  $k = 22$  ( $ka = 2.23$ ), at  $t = 0, 2.5, 12.5$  and  $20.5$ , viewed orthographically at an angle of  $45^\circ$  from the  $x$ -axis and  $z$ -axis. Colour shading indicates depth (dark contours near the bottom of the filament and light contours). In the second panel, the black lines highlight the central and top/bottom contours at  $t = 2.5$ . (Colour online.)

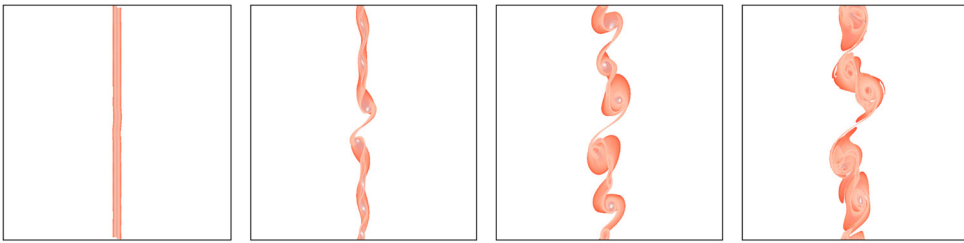


**Figure 11.** Top view on the filament's bounding contours for  $\lambda = 0.1$  and a polychromatic disturbance  $d(x)$  at  $t = 0, 4, 6$  and  $8$ . Colour shading indicates depth (dark contours near the bottom of the filament and light contours). (Colour online.)

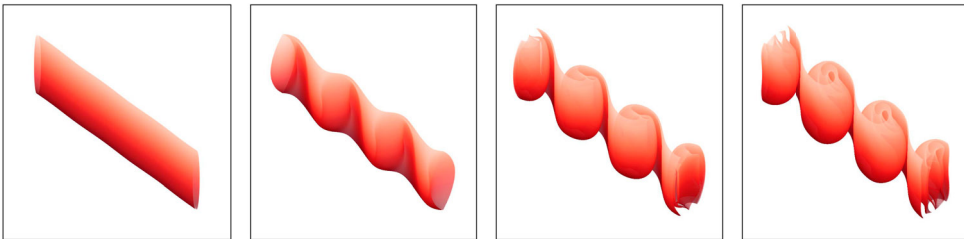


**Figure 12.** Filament's bounding contours from  $\lambda = 0.1$ , perturbed by a monochromatic wave  $k = 3$  ( $ka = 0.332$ ), at  $t = 0, 5, 8$  and  $10$ , viewed orthographically at an angle of  $45^\circ$  from the  $x$ -axis and  $z$ -axis. Colour shading indicates depth (dark contours near the bottom of the filament and light contours). (Colour online.)

larger wavenumber, corresponding to an even smaller growth rate. Figures 10 and 11 show the evolution of the filament for  $ka = 2.23$ , corresponding to  $k = 22$  in the computational box. As shown in figure 5, the mode affect mostly the top and bottom tips of the filament. This is stressed in the second panel of figure 10 where the top, bottom and centre bounding contours are highlighted. Kelvin–Helmholtz billows have formed on the top and bottom tips of the filament while the perturbation has little grown in the central region of the

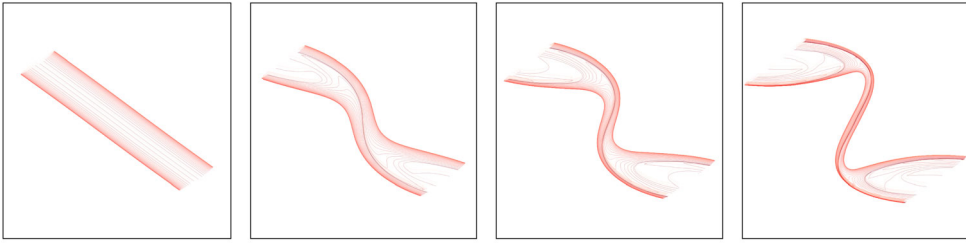


**Figure 13.** Filament's bounding contours from  $\lambda = 10$ , perturbed by a monochromatic wave  $k = 1$  ( $ka = 0.632$ ), at  $t = 0, 90, 100$  and  $110$ , viewed orthographically at an angle of  $45^\circ$  from the  $x$ -axis and  $z$ -axis. Colour shading indicates depth (dark contours near the bottom of the filament and light contours). (Colour online.)

filament. Again, as the flow evolves, lower wavenumber modes grow from the perturbations generated by the nonlinear evolution of the filament. The late evolution of the flow is dominated by a mode  $k = 5$ , the most amplified mode available in the periodic box.

The last numerical experiment for  $\lambda = 0.1$  shows the evolution of the same filament for a polychromatic forcing given by

$$d(x) = \epsilon \sum_{k=1}^{10} \sin(ky + \phi_k), \quad (15)$$

where  $\phi_k$  is a random phase,  $0 \leq \phi_k \leq 1$  and  $\epsilon = 0.002$ . The purpose of the polychromatic perturbation is to confirm that the linearly most amplified mode dominates the early nonlinear evolution of the flow and the later stage evolution. It should be noted that all the modes in the sum are unstable. At early stage, five asymmetric billows develop, consistent with the prevalence of the mode  $k = 5$ .

We finally consider the evolution of the filament with  $\lambda = 10$ . Here  $a = 0.632$  and  $b = 0.0632$ . Results are shown in figure 13. The flow is initially perturbed by a uniform amplitude sine wave with  $ka = 0.632$ , corresponding to  $k = 1$  in the computational box. Again, the filament rolls-up to form billows. Recall that the shear inside the filament,  $s = 2\pi/(1 + \lambda)$ , and the instability growth rates decrease as  $\lambda$  increases. Hence the roll-up occurs on a much larger time scale compared to the cases with  $\lambda = 0.1$ . It should be noted that, as the periodic billows roll-up, a strained filament, often referred to as a braid in the literature, forms between the billows. We will illustrate the late fate of the filament in section 4.

#### 4. Linear evolution of a filament in pure strain

We next consider the evolution of the perturbation on the boundary of the filament when the strain is applied. Now both the width of the filament and the perturbation wavenumber are time dependent and evolve according to

$$a(t) = a_0 \exp(-\gamma t), \quad k(t) = k_0 \exp(-\gamma t), \quad (16)$$

where  $a_0 = a(t = 0)$  and  $k_0 = k(t = 0)$  are the initial half-width of the filament and initial perturbation wavenumber respectively. Following Dritschel *et al.* (1991) and Harvey and

Ambaum (2010), it is natural to write the  $y$ -position of the boundary of the filament as

$$y(\theta, t) = \exp(-\gamma t) (\bar{y}(\theta) + \epsilon \eta(x, \theta, t)), \quad (17)$$

where  $\bar{y} = a \cos \theta$  is the initial position of the unperturbed filament, and  $\epsilon \eta \exp(-\gamma t)$  is the perturbation's amplitude. The kinematic boundary condition

$$\frac{D}{Dt} (\exp(-\gamma t) (\bar{y}(\theta) + \epsilon \hat{\eta})) = v_g(x, y(\theta), t) - \gamma y(\theta) \quad (18)$$

is then expanded and linearised with respect to  $\epsilon$ . We therefore obtain, at  $O(\epsilon)$ , for a monochromatic wave form  $\eta(x, \theta, t) = \hat{\eta}(\theta, t) \exp(ikx)$ , the following linearised equation for the complex amplitude  $\hat{\eta}$ .

$$\frac{\partial \hat{\eta}(\theta)}{\partial t} = -ik \left( \bar{u}_g(t) \hat{\eta}(\theta, t) + \frac{q}{4\pi} \int_{-\pi/2}^{3\pi/2} 2\hat{\eta}(\theta', t) K_0(k(t)\varrho) b \cos(\theta') d\theta' \right), \quad (19)$$

where

$$\bar{u}_g(t) = -\frac{qb}{(a(t) + b)} \bar{y}(\theta) \exp(-\gamma t). \quad (20)$$

Although the equation is very similar to equations (12) and (13), it has no simple analytical solution since the coefficients are now time dependent. Recall that the actual complex amplitude of the perturbation is  $\epsilon \exp(-\gamma t) \hat{\eta}$ . We denote  $\hat{\eta}_{re}$  and  $\hat{\eta}_{im}$  the real and imaginary parts of  $\hat{\eta} = \hat{\eta}_{re} + i\hat{\eta}_{im}$ . The complex equation is marched in time using a fourth-order Runge-Kutta scheme with  $\Delta t = 0.01$  and  $q = 1$ , for various values of  $\gamma$ . Again, the surface of the filament is discretised using  $n$  contours, and we define the perturbation amplitude

$$A(t) = \exp(-\gamma t) \sqrt{\sum_{i=1}^n \hat{\eta}_{i,re}^2(t) + \hat{\eta}_{i,im}^2(t)} = \exp(-\gamma t) |\hat{\boldsymbol{\eta}}|, \quad (21)$$

where  $\hat{\boldsymbol{\eta}} = (\hat{\eta}_i)_{1 \leq i \leq n} = (\hat{\eta}_{i,re} + i\hat{\eta}_{i,im})_{1 \leq i \leq n}$ . We denote  $A_0 = A(t = 0)$ . It should be noted that  $A(t)$  depends on (i) the value of  $\gamma$ , also on (ii) the choice of the initial aspect ratio of the filament,  $\lambda_0 = a_0/b$ , (iii) the starting wavenumber  $k_0$  and (iv) the initial deformation  $\hat{\eta}(\theta, t = 0)$ .

In Dritschel *et al.* (1991), the two-dimensional filament is fully determined by two contours and there is no such parameter as  $\lambda_0$ . Therefore in this context, the task is to find, for a given  $k_0$  and  $\gamma$  the initial perturbation  $(\hat{\eta}_1, \hat{\eta}_2)$  for the two contours which maximises, over time, the amplification of the perturbation. In practice, this means finding the phase between the two contour perturbations which maximise the amplification of the perturbation. Due to the size of the three-dimensional problem with  $n = 2000$  contours, finding the  $n-1$  initial phases which maximise over time the amplitude is impractical. An alternative solution is to start, for a given  $\lambda_0$ , with a perturbation with a wavenumber  $0 < k_0 < k_c$ , where  $k_c$  is the cutoff wavenumber. Then it is natural to use the deformation eigenmode associated with the largest growth rate for  $k_0$ , as found in the linear stability analysis for the astatic filament of aspect ratio  $\lambda_0$  detailed in section 3.1.

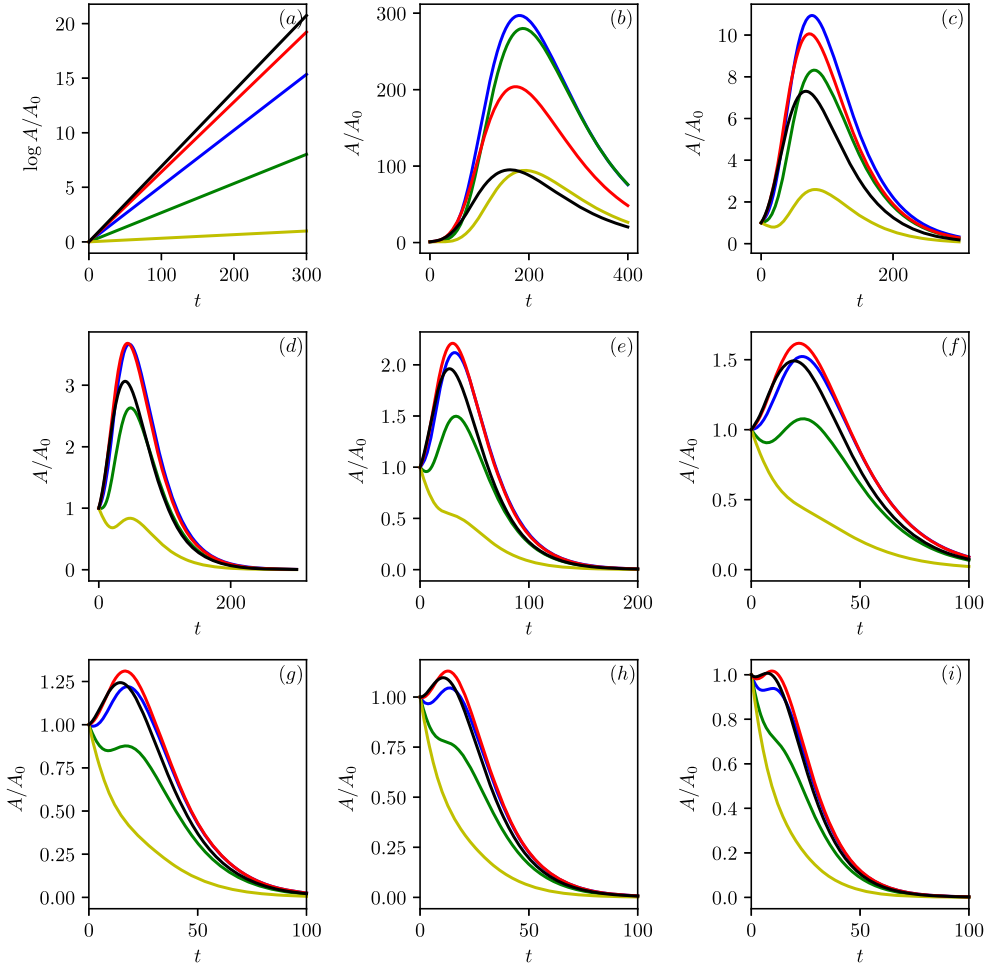


**Figure 14.** Normalised magnitude  $A/A_0$  of the complex perturbation amplitude  $\exp(-\gamma t)\hat{\eta}$  versus  $t$  for  $\lambda_0 = 1$ . Panel (a) shows  $\log(A/A_0)$  versus  $t$  for  $\lambda_0 = 1$  and  $\gamma = 0$ . Panels (b)–(i) show  $A/A_0$  versus  $t$  for  $\lambda_0 = 1$ , (b)  $\gamma = 0.01$ , (c)  $\gamma = 0.02$ , (d)  $\gamma = 0.03$ , (e)  $\gamma = 0.04$ , (f)  $\gamma = 0.05$ , (g)  $\gamma = 0.06$ , (h)  $\gamma = 0.07$ , (i)  $\gamma = 0.08$  and  $k_0 a_0 = 0.676$  (black),  $0.8$  (red),  $0.9$  (blue),  $1.0$  (green),  $1.06$  (yellow). (Colour online.)

Note that when the strain is applied, the normalised wavenumber  $k(t)a(t) \propto \exp(-2\gamma t)$ , hence it is impossible for  $ka$  to remain close to  $k_m a \forall t$ , where  $k_m = k_m(a)$  is the wavenumber of the most amplified mode in the quasi-static situation discussed in section 3.1. Selecting  $k_0 a_0 > k_m a_0$  means that  $k(t)a(t)$  matches  $k_m(a)a(t)$  of the equivalent quasi-static filament of section 3.1, for only one value of  $t^* > 0$ , hence a specific value of  $a(t^*)$ . The time  $t^*$  and filament's half-width  $a(t^*)$  depend on  $k_0$ . Finally, it should be noted that using  $k_0 = k_m = 0.676$  for  $\lambda_0 = 1$ , corresponds to starting the simulation with the most amplified mode for the filament at  $t = 0$ .

We first present the evolution of  $A(t)$  for  $\lambda_0 = 1$  and various values of  $k_0$  and  $\gamma$  in figure 14. For  $\gamma = 0$  we naturally simply recover the exponential growth of the eigenmode for  $k_0$ . For  $\gamma \neq 0$ , in all cases considered, the amplitude of the perturbation eventually vanishes to zero as  $t \rightarrow \infty$  in the linear dynamics. However, for small value of  $\gamma$ , the amplitude

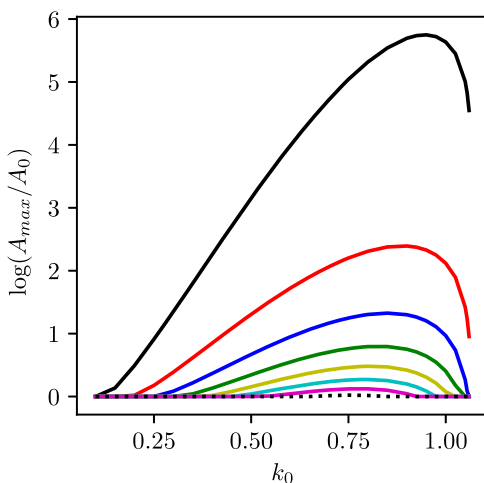
of perturbation can reach very large values. In the fully nonlinear dynamics, this is likely to allow nonlinear, irreversible deformations of the filament to occur.

For  $\gamma = 0.01$ , and  $k_0a = 0.676, 0.8, 0.9$  and  $1.0$ ,  $A(t)$  always reached a maximum about 2 orders of magnitude larger than  $A_0$ . Using an initial perturbation with  $k_0a \lesssim 1$  optimises the amplification. This is explained by the fact that the largest growth rate of perturbation for the equivalent quasi-static filament, initially increases as  $ka$  decreases from 1 for  $\lambda \leq 1$ . For  $k_0a = 0.676$ , the amplification is initially large as the growth rate of the equivalent quasi-static filament is maximum, but the latter decreases as  $ka$  decreases. For  $k_0a = 1.06$ , close the normalised cutoff wavenumber, the growth rate of the most unstable mode is small, strongly limiting the growth of the perturbation in the strained filament. The initial perturbation, i.e. the eigenmode for  $k_0a = 1.06$  may also be far from the optimal perturbation for  $ka \ll k_0a$ .

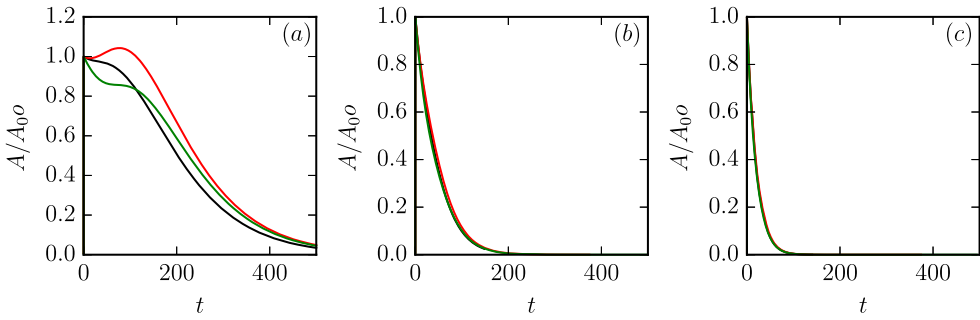
As we increase  $\gamma$  the overall maximum amplification decreases, as expected, and the amplitude of the perturbation may in fact initially decrease. For example, for  $\gamma \geq 0.03$  and  $k_0a = 1.06$ , the amplitude of the perturbation is always less than the initial perturbation. It is monotonously decreasing for  $\gamma \geq 0.04$  and  $k_0a = 1.06$ . Perturbations for all  $k_0a$  shown follow the same trends as  $\gamma$  increases. No significant amplification is seen for  $\gamma = 0.08$ . Even for  $\gamma \geq 0.03$ , an initial small perturbation would likely remain small as the perturbation is never amplified by an order of magnitude.

Figure 15 gives the maximum amplification, over time, for  $\lambda_0 = 1$  as a function of  $k_0$  for various values of  $\gamma$ . For all  $\gamma$ , the maximum is achieved for  $k_0 \lesssim 1$ . These cases appear to optimise the time period when the filament is narrow enough (small  $\lambda$ ) to exhibit a large inner shear, while  $ka$  remains close to  $k_m a$ . The results also confirm that any strain rate larger than 0.03 is enough to significantly impede the growth perturbations.

We then explore a couple of different values of  $\lambda_0$ . We start with  $\lambda_0 = 10$ . Results are presented in figure 16 for  $\gamma \in \{0.01, 0.03, 0.06\}$  and  $k_0a \in \{0.6, 0.8, 1\}$ . First, recall that the growth rate of the equivalent quasi-static filament decreases as  $\lambda$  increases. Hence, it is expected that initially the evolution of a flat ( $\lambda \gg 1$ ) filament is mostly dominated by the



**Figure 15.** Natural logarithm of the normalised maximum amplitude  $\log(A_{max}/A_0)$  versus the initial wavenumber  $k_0$  for  $\lambda_0 = 1$  and for  $\gamma = 0.01$  (solid black), 0.2 (solid red), 0.3 (solid blue), 0.4 (solid green), 0.5 (solid yellow), 0.6 (solid cyan), 0.7 (solid magenta), 0.8 (dashed black). (Colour online.)



**Figure 16.** Normalised magnitude  $A/A_0$  of the complex perturbation amplitude  $A = \exp(-\gamma t)|\hat{\eta}|$  versus  $t$  for  $\lambda_0 = 10$ : (a)  $\gamma = 0.01$ , (b)  $\gamma = 0.03$ , (c)  $\gamma = 0.06$ , and  $k_0 a_0 = 0.6$  (black),  $0.8$  (red) and  $1$  (green). (Colour online.)

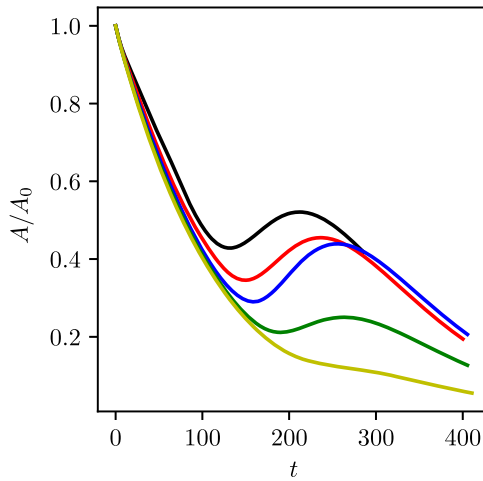


**Figure 17.** Evolution of the perturbation amplitude  $A(t)$  for  $\lambda_0 = 10$ ,  $k_0 a_0 = 5$  (black),  $7$  (red)  $9$  (blue),  $11$  (green) and  $13$  (yellow). (Colour online.)

stabilising effect as shown in figure 16 for  $\gamma \geq 0.01$ . The filament's aspect ratio,  $\lambda$ , decreases with time as the filament is stretched more slowly than the normalised wavenumber  $ka$ . And although the shear rate increases in the filament it remains bounded. Hence overall, the perturbation with vanishing  $ka$  can no longer be significantly amplified. To obtain any significant amplification over time, one would need to introduce a perturbation with a much larger wavenumber  $k \gg k_c(a_0)$  of the equivalent quasi-static filament. That way we could have  $ka \simeq k_m a$  for small  $\lambda$ , hence potentially a strong amplification of the perturbation. Numerical experiments indicate that we can observe a moderate growth of the amplitude of the perturbation at intermediate times, after an initial phase of decrease of the amplitude in such cases. However, by starting from  $k \gg k_c(a_0)$ , we have no information on an approximate optimal initial perturbation. The number of contours discretising the filament makes a systematic investigation for the optimal perturbation impractical. By simply uniformly shifting the filament by taking  $(\hat{\eta}_i)_{1 \leq i \leq n}$  a constant real vector, the amplification is not enough to recover the initial amplitude as shown in figure 17.



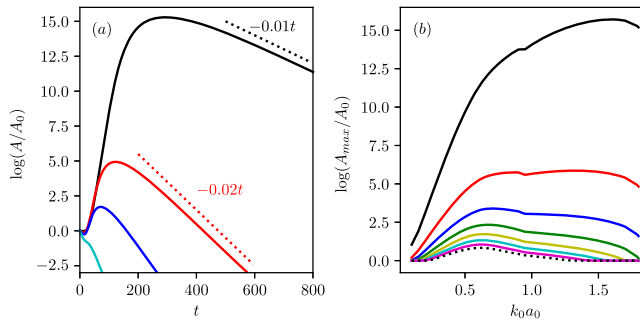


**Figure 18.** (a) Natural logarithm of the normalised magnitude  $\log(A/A_0)$  of the complex perturbation amplitude  $A(t) = \exp(-\gamma t)\hat{\eta}$  versus  $t$  for  $\lambda_0 = 0.2$ .  $\gamma = 0.01$  (black), 0.02 (red), 0.03 (blue) and 0.06 (cyan) and  $k_0 a_0 = 1.79$ , (b) natural logarithm of the normalised maximum amplitude  $\log(A_{max}/A_0)$  versus the initial wavenumber  $k_0$  for  $\lambda_0 = 0.2$  and for  $\gamma = 0.01$  (solid black), 0.2 (solid red), 0.3 (solid blue), 0.4 (solid green), 0.5 (solid yellow), 0.6 (solid cyan), 0.7 (solid magenta), 0.8 (dashed black). (Colour online.)

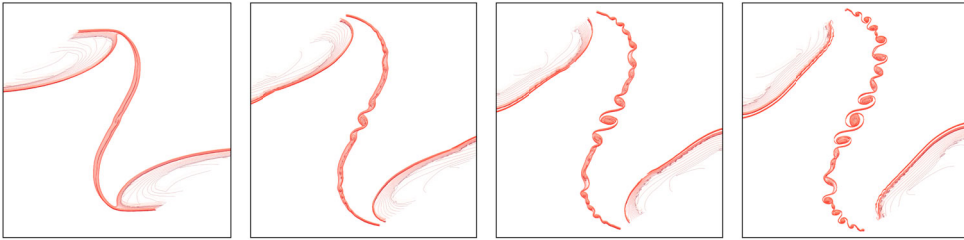


**Figure 19.** Filament's bounding contours from  $a/b = 10$ , perturbed by a monochromatic wave  $k = 1$  ( $ka = 0.63$ ), at  $t = 120, 128, 133$  and  $138$ , viewed orthographically and at angle of  $45^\circ$  from the  $x$ -axis and the  $z$ -axis. (Colour online.)

For  $\lambda_0 = 0.2$ , the maximum amplification is enhanced as the inner shear is intense. The range of  $ka$  where unstable modes are found is also larger. We therefore can start the simulation from a  $k_0 a_0$ , within the unstable range, larger to the one used in the previous cases. The normalised wavenumber  $ka$  also remains in the range where modes can be strongly amplified for longer. As  $t \rightarrow \infty$ ,  $ka \rightarrow 0$  and that the filament is no longer able to strongly amplify the perturbation. Recall that for the equivalent quasi-static filament,  $\sigma_i \rightarrow 0$  as  $k \rightarrow 0$ . Hence the evolution of the amplitude of the perturbation is simply dominated by the exponential decrease of the amplitude  $\propto \exp(-\gamma t)$  as confirmed in panel (a) of figure 18. Panel (b) of figure 18 shows the maximum amplification over time vs  $k_0 \in (0, k_c)$  where  $k_c$  is the cutoff wavenumber for the equivalent quasi-static filament for  $\lambda_0 = 0.2$ . The amplification achieved is overall higher than for  $\lambda_0 = 1$  as expected. The maximum normalised amplification  $A_{max}/A_0 \simeq 29$  for  $\gamma = 0.03$ , but only 2.3 for  $\gamma = 0.08$ .

An example of the nonlinear roll-up of a weakly strained filament is presented in figure 19. The figure shows the late evolution of the filament first shown in figure 13. As the primary billows roll-up and saturate, the braid connecting two neighbouring billows in the periodic flow destabilises. The braid is nothing but a filament itself, subjected to the

weak strain induced by the rotation of the primary billows. In this case, the strain is too weak to stabilise the braid and it rolls up as a series of secondary billows.

## 5. Conclusion

We have studied the behaviour of a three-dimensional filament of uniform quasi-geostrophic potential vorticity in strain. We have first shown that the stability of the filament depends on this cross-sectional aspect ratio. First, small width-to-height aspect ratio ( $\lambda$ ) filaments experience a larger inner shear compared to filaments with large  $\lambda$ . Therefore the growth rate of unstable modes is typically larger for small  $\lambda$  than for large  $\lambda$ . Filaments with small  $\lambda$  are also unstable to perturbation within a larger range of normalised wavenumbers, compared to the ones with larger  $\lambda$ . They are also sensitive to more unstable modes, including a tilting mode. Their increased sensitivity to vertical shear also allows modes of instability to primarily affect their top and bottom tips.

As in the two-dimensional filament, the strain has a two-fold stabilising effect of the filament by (i) making the perturbation's wavenumber go to zero and (ii) actively reducing the amplitude of the perturbation. It can, however, increase the responsiveness of the filament by increasing the self-induced inner shear. This increase, contrarily to the case of the surface quasi-geostrophic potential temperature filament, remains bounded. Eventually, in the linear dynamics, the strain is stabilising.

A filament can still amplify a perturbation significantly when subjected to a weak strain, as, in the linear dynamics the amplitude of the perturbation can increase by several orders of magnitude. However, even a relatively weak strain with a strain rate of as little as 3% of the filament's PV,  $q$ , can significantly impede the growth of perturbation. Arguably no initially small perturbation could trigger irreversible nonlinear deformations in a strain whose strain rate exceeds 8% of  $q$ .

A possible extension of this study is the inclusion of ageostrophic effects and of inertia-gravity waves on sub-mesoscale filaments. For example, whether the filament loses significant energy by spontaneously generating waves, or whether the filament remains largely balanced is an important question.

## Disclosure statement

No potential conflict of interest was reported by the author(s).

## Data availability statement

The data repository for this paper can be found at <https://doi.org/10.17630/e920829b-60b2-49af-9575-0fdc0e2c8356>.

## ORCID

Jean N. Reinaud  <http://orcid.org/0000-0001-5449-6628>

## References

Bambrey, R.R., Reinaud, J.N. and Dritschel, D.G., Strong interactions between two co-rotating quasi-geostrophic vortices. *J. Fluid Mech.* 2007, **592**, 117–133.

- Dritschel, D.G., The instability and breakdown of tall columnar vortices in a quasi-geostrophic fluid. *J. Fluid Mech.* **1996**, **328**, 129–160.
- Dritschel, D.G. and Ambaum, M.H.P., A contour-advective semi-Lagrangian numerical algorithm for simulating fine-scale conservative dynamical fields. *Quart. J. Roy. Meteorol. Soc.* **1997**, **123**, 1097–1130.
- Dritschel, D.G., Haynes, P.H., Jukes, M.N. and Shepherd, T.G., The stability of a two-dimensional vorticity filament under uniform strain. *J. Fluid Mech.* **1991**, **230**, 647–665.
- Harvey, B.J. and Ambaum, M.H.P., Instability of surface-temperature filaments in strain and shear. *Q. J. R. Meteorol. Soc.* **2010**, **136**, 1506–1513.
- Kevlahan, N.K.R. and Farge, M., Vorticity filaments in two-dimensional turbulence: creation, stability and effect. *J. Fluid Mech.* **1997**, **346**, 49–76.
- Kirchhoff, G., *Mechanik*, **1876** (Drick und Verlag von B. G. Teubner: Leipzig).
- Lamb, H., *Hydrodynamics*, 4th ed., **1916** (Cambridge University Press: Cambridge).
- Reinaud, J.N., Stability of filaments of uniform quasi-geostrophic potential vorticity. *Geophys. Astrophys. Fluid Dyn.* **2020**, **114**, 798–820.
- Reinaud, J.N. and Dritschel, D.G., The critical merger distance between two co-rotating quasi-geostrophic vortices. *J. Fluid Mech.* **2005**, **522**, 357–381.
- Reinaud, J.N. and Dritschel, D.G., Destructive interactions between two counter-rotating quasi-geostrophic vortices. *J. Fluid Mech.* **2009**, **639**, 195–211.
- Reinaud, J.N., Dritschel, D.G. and Koudella, C.R., The shape of vortices in quasi-geostrophic turbulence. *J. Fluid Mech.* **2003**, **474**, 175–191.
- Vallis, G.K., *Atmospheric and Oceanic Fluid Dynamics: Fundamentals and Large-scale Circulation*, **2006** (Cambridge University Press: Cambridge).

## Appendix. Linear stability: convergence and accuracy

Figure A1 compares the largest growth rates obtained for  $\lambda = 0.1$  using  $n = 360, 500, 1000, 2000$  and  $4000$ . Overall all results agree well, including in reproducing the long tail of unstable modes for  $ka > 1.1$ , absent for small  $\lambda$ . Using  $n = 2000$  in the study is a good compromise between computational cost and accuracy. Choosing a lower value for  $n$  mainly affects the results for  $k \simeq 0$  and  $k \simeq k_c$  regions where  $\sigma_i$  is small, leading to moderate relative errors.

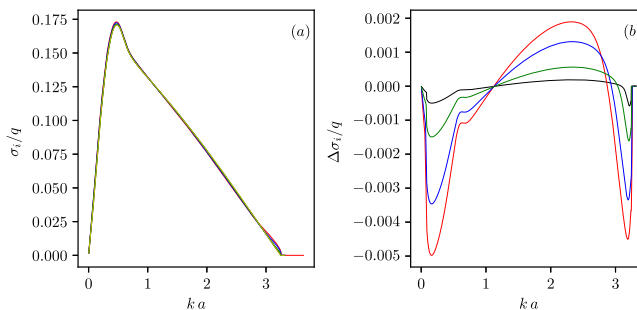


**Figure A1.** (A) Largest normalised growth rate  $\sigma/q$  versus  $ka$  for  $\lambda = 0.1$  and  $n = 360$  (red),  $500$  (blue),  $1000$  (green),  $2000$  (black), and  $4000$  (yellow). (b) Difference between the growth rate calculate using  $n = 360$  (red) or  $n = 500$  (blue) or  $n = 1000$  (green) or  $n = 2000$  (black) and the growth rate calculated for the highest resolution  $n = 4000$ . (Colour online.)